

Supplemental Material for:

“Hydrothermal alteration can result in pore pressurization and volcano instability”

By Michael J. Heap, Tobias Baumann, H. Albert Gilg, Stephan Kolzenburg, Amy Ryan, Marlène Villeneuve, Kelly Russell, Lori A. Kennedy, Marina Rosas-Carbajal, and Michael A. Clynne

1. Sample locations and photographs

Fieldwork was conducted in June 2019 at Chaos Crags (Lassen Volcanic Center, USA) (Fig. S1). In total, four blocks were collected: CCC (a relatively unaltered block taken from the Chaos Jumbles deposit; Fig. S1) and three blocks selected due to their visual differences in alteration (CC4A, CC4B, and CC10). The altered blocks were collected in-situ (i.e. from outcrops, not loose blocks) from the altered carapace of the dome that now forms the collapse scar. Visually altered rock outcrops (based on their color) pepper the now-exposed carapace of the dome. Blocks CC4A and CC4B were white-yellow in color and CC10 was gray-purple. The sampling locations for all four blocks are indicated in Fig. S1B and photographs of the sampling sites are available in Fig. S1A (for CCC), Fig. S2A (for CC4A and CC4B), and Fig. S2B (for CC10). Photographs of cylindrical samples (20 mm in diameter) prepared from each of the blocks for the laboratory testing are provided as Fig. S2C.

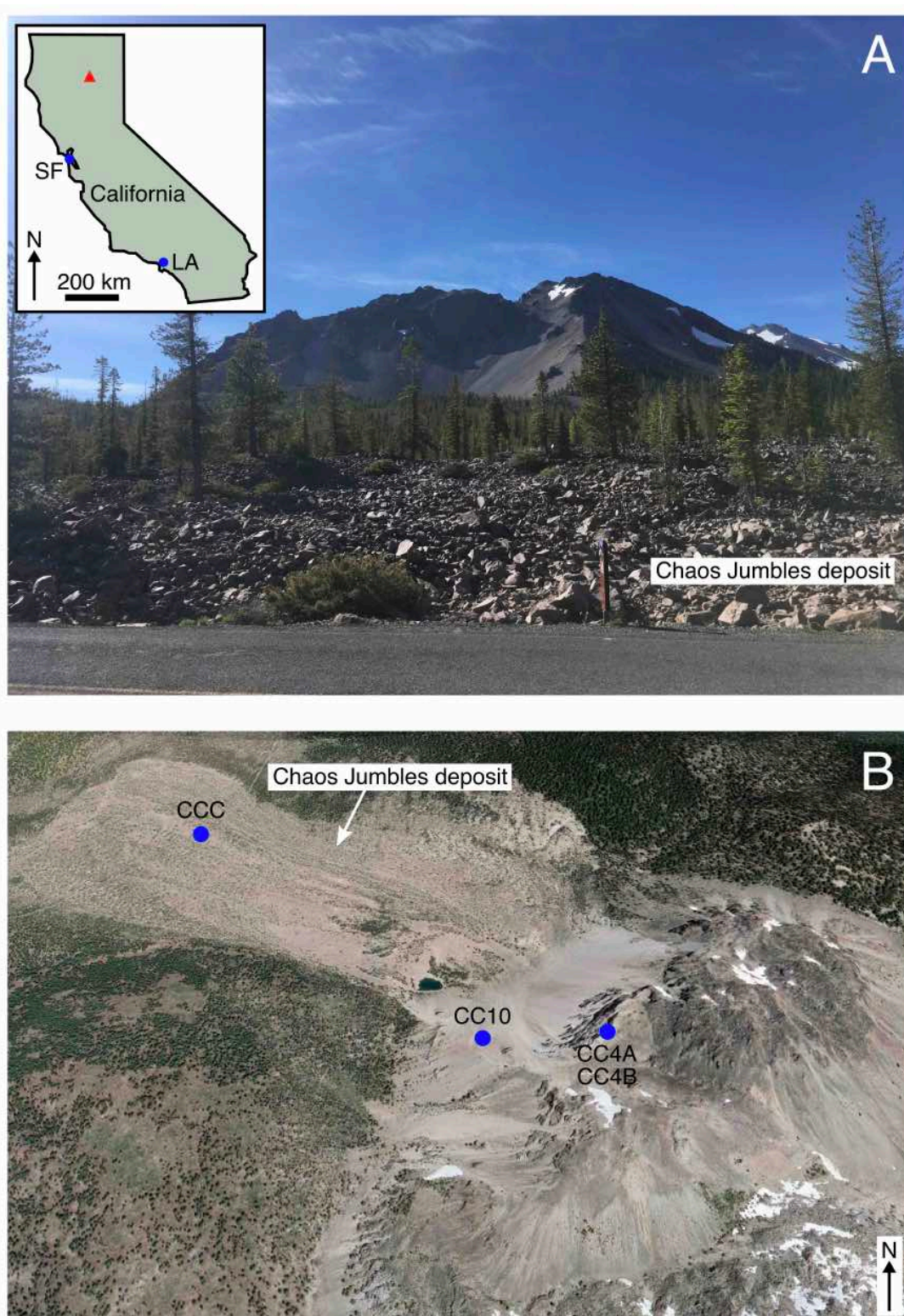


Figure S1. A: Photograph of Chaos Crags (Lassen Volcanic Center, USA). Inset shows the location of Chaos Crags (red triangle) in the state of California (USA). Sample CCC was collected from this location. B: Google Earth® image showing the sampling sites for the samples (CCC, CC4A, CC4B, and CC10).

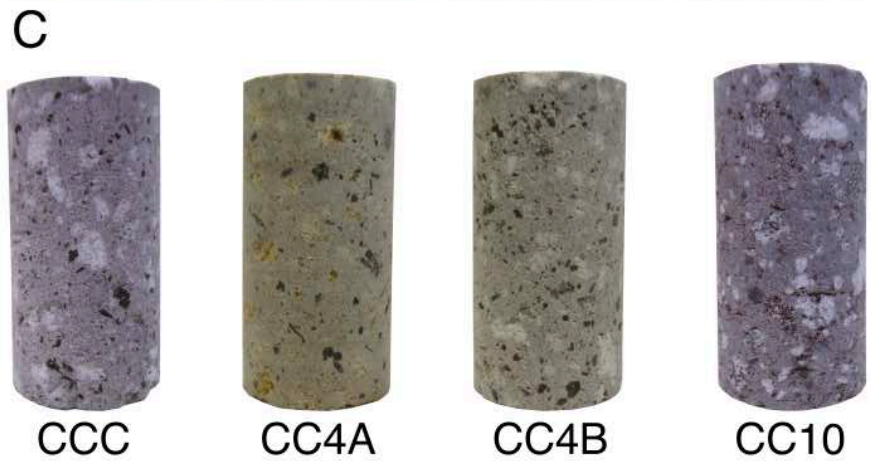


Figure S2. A: Photograph of the collection site for samples CC4A and CC4B. B: Photograph of the collection site for sample CC10. C: Photographs of the 20 mm-diameter core samples prepared for the laboratory experiments.

2. Backscattered scanning electron and polarized light microscopy

Backscattered scanning electron microscope (SEM) images of each of the four blocks (CCC, CC4A, CC4B, and CC10) are presented in Fig. S3 (porosity = black). All blocks are porphyritic rhyodacitic dome lavas that contain often glomerophyric phenocrysts (typically 1-2 mm in length, but can reach lengths of up to 5 mm) within a crystallized groundmass. Microcracks are also present in all blocks. Notably, samples CC4A and CC4B contains pore- and microcrack-filling alteration, as discussed in the main manuscript. An early stage of porosity infill by cristobalite and later colloform hematite and kaolinite can be observed (Fig. S4).

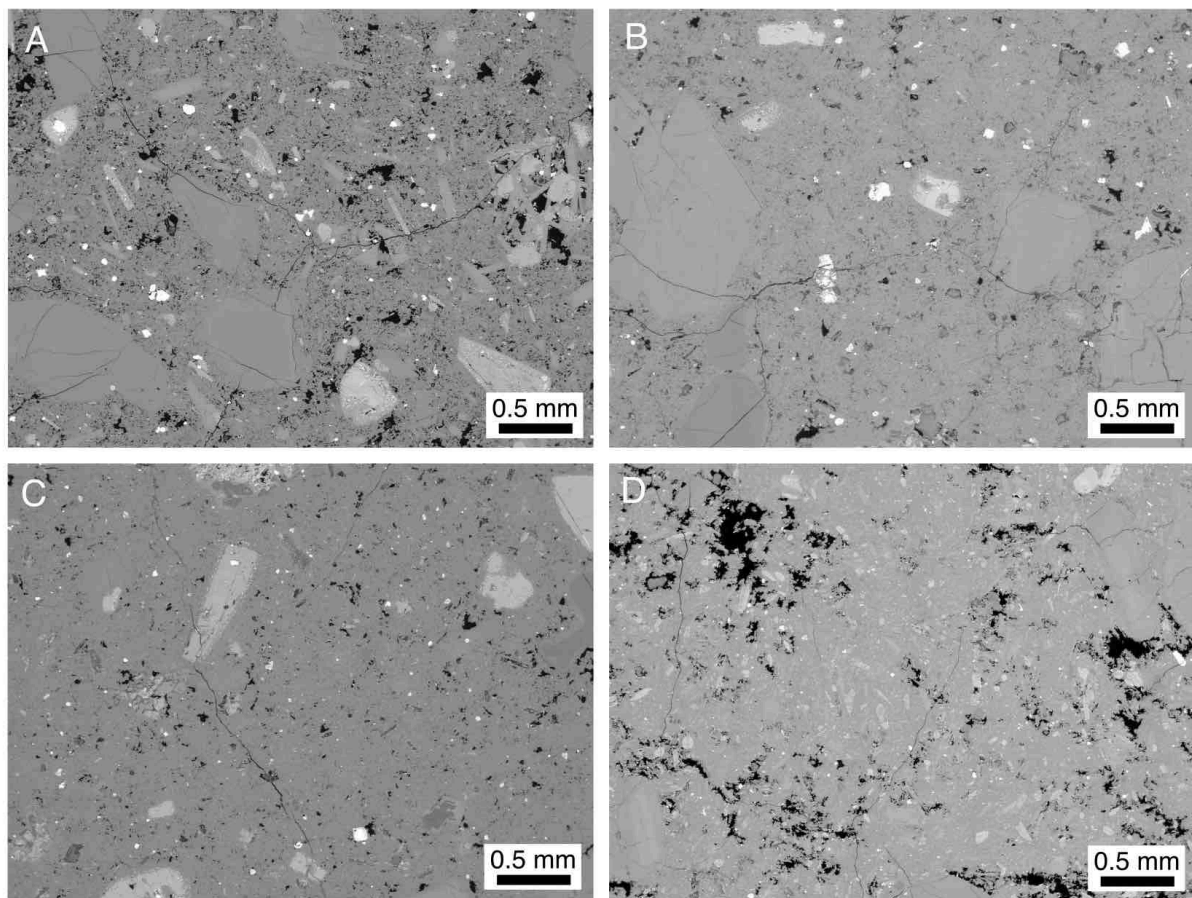


Figure S3. A: Backscattered scanning electron microscope (SEM) image of sample CCC. B: SEM image of sample CC4A. C: SEM image of sample CC4B. D: SEM image of sample CC10.

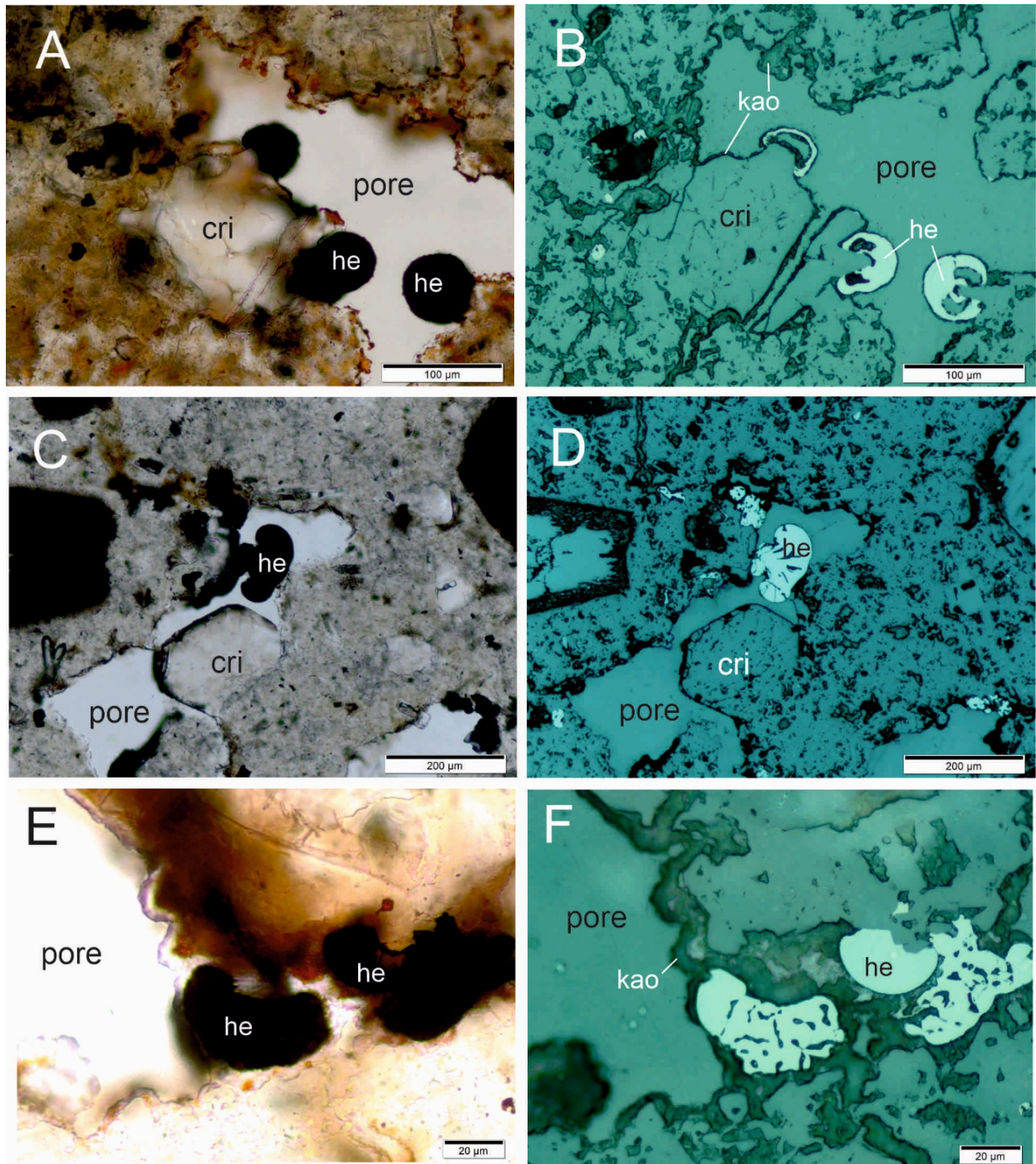


Figure S4. A, C, E: transmitted light micrographs, B, D, F: reflected light micrographs of sample CC4A showing pore filling by early cristobalite (cri) and later colloform hematite (he) and kaolinite (kao).

3. X-ray powder diffraction

The mineral phase assembly of the four blocks was quantified using X-ray powder diffraction (XRPD) on powdered offcuts of the samples. Powdered offcuts of the core material were ground with 10 ml of isopropyl alcohol for 8 min in a McCrone Micronizing Mill using ZrO₂ cylinder elements. The XRPD analyses were performed on powder mounts

using a Bruker D8 Advance Eco X-ray diffractometer (CuK α , 40 kV, 25 mA, 2°–75° 2 θ , 0.01° step size, 15 mm irradiated length, 2.5° primary and secondary sollers and a LynxEye XE-T detector). The phases in the whole rock powders were then quantified using the Rietveld program BGMN (Bergmann et al., 1998) and the Profex graphical user interface (Döbelin and Kleeberg, 2015). To identify clay minerals, we also separated < 2 μ m fractions by gravitational settling and prepared oriented mounts that were X-rayed in an air-dried state, an ethylene-glycolated state, and following exposure to 550 °C. The results are shown in Table S1. We highlight that only CC4A and CC4B contain notable smectite and kaolinite.

Table S1. Mineral contents (in wt.%) for each of the four blocks used in this study, measured by X-ray powder diffraction.

	CCC	CC4A	CC4B	CC10
Plagioclase	52.6	36.3	42.9	58.9
K-feldspar	16.8	14.6	16.7	10.5
Quartz	17.8	25.4	17.8	4.0
Cristobalite*	5.2	9.8	8.7	22.2
Biotite	2.5	3.1	3.5	0.2
Hornblende	1.0	1.7	1.8	1.0
Clinopyroxene	2.3	1.7	2.2	
Magnetite	0.3	0.6	0.5	1.0
Hematite* **	1.2	0.6	0.8	2.1
Smectite**	-	1.3	0.9	-
Kaolinite**	-	4.8	4.2	-

* early alteration phase, ** late alteration phase

4. Expanded experimental methods

4.1 Sample preparation

Cylindrical core samples were cored from the four blocks collected during the field campaign (CCC, CC4A, CC4B, and CC10), in the same direction, using a diamond-tipped core drill with an internal diameter of 20 mm. These samples were then cut and precision-ground using a diamond-tipped grinding wheel, so that their end-faces were flat and parallel, to a nominal length of 40 mm. The samples were then washed using tap water, dried on a hotplate for several days, and then, finally, dried in a vacuum-oven at 40 °C for at least 48 hours.

4.2 Porosity and permeability

The connected porosity of each sample (20 mm-diameter cylindrical core samples) was measured using the bulk sample volume, measured using digital calipers, and the skeletal sample volume measured using an AccuPyc II helium pycnometer from Micromeritics®. The permeability of each sample (20 mm-diameter cylindrical core samples) was measured using a benchtop gas (nitrogen) permeameter (Heap and Kennedy, 2016) and a confining pressure of 1 MPa. Permeability was measured using either the steady-state method (for high-permeability samples) or the pulse-decay method (for low-permeability samples). For the steady-state experiments, steady-state volumetric flow rates were measured (using a

BRONKHORST gas flow meter) for six different pore pressure differentials (measured using a KELLER pressure transducer). Pulse-decay measurements were performed by monitoring the decay of a pressure differential (starting pressure differential = 0.2 MPa) over time. These data were used to calculate permeability using Darcy's law. When necessary, these data were corrected using the Klinkenberg and Forchheimer corrections (for more details, see Heap et al., 2017).

4.3 Uniaxial compressive strength

The uniaxial compressive strength (UCS) experiments were performed on select samples (20 mm-diameter cylindrical core samples) of each of the blocks using a uniaxial loadframe (see Heap et al. (2014) for a schematic) and a constant axial strain rate of 10^{-5} s^{-1} . Samples were first dried in a vacuum-oven at 40 °C for at least 48 hours. Axial displacement and axial load were measured using a linear variable differential transducer (LVDT) and a load cell, respectively. Axial displacement (minus the displacement accumulated within the load chain) and axial load were converted to axial strain and axial stress using the sample dimensions. A lubricating wax was used on the end-faces of each sample to avoid problems with friction between the sample and the piston. The static Young's modulus was determined from the elastic portion of the uniaxial stress-strain curves (as in Heap et al., 2020).

4.4 Triaxial deformation experiments

The samples were first vacuum-saturated in deionized water. Samples (20 mm-diameter cylindrical core samples) were then inserted into a rubber jacket and placed inside a pressure vessel (see Farquharson et al. (2017) for a schematic of the triaxial press). The samples were then taken to the target confining and pore fluid pressures using servo-controlled pumps. Once equilibrated to the pressure conditions, the samples were deformed at a constant axial strain rate of 10^{-5} s^{-1} until macroscopic failure. Axial displacement and axial load were measured using a linear variable differential transducer (LVDT) and a load cell, respectively. Axial displacement (minus the displacement accumulated within the load chain) and axial load were converted to axial strain and axial stress using the sample dimensions. We assume here a simple effective pressure law where the effective pressure, P_{eff} , is the confining pressure, P_c , minus the pore fluid pressure, P_p . Triaxial compression experiments were performed on water-saturated samples of the least (sample CCC) and most altered (sample CC4A) blocks using a pore fluid (water) pressure of 10 MPa and confining pressures between 12.5 and 30 MPa.

5. Experimental data

Tabulated experimental data (connected porosity, permeability, Young's modulus, and uniaxial compressive strength) are provided in Table S2. Variations in the porosity of samples cored from block CC4A is likely the result of sample-to-sample variability. Importantly, the permeabilities of the eight CC4A samples are all low (see Table S2). Young's modulus and uniaxial compressive strength are plotted as a function of connected porosity in Fig. S5. Fig.

S6 presents the triaxial deformation data (stress-strain curves) for CCC (relatively unaltered) and CC4A (highly altered). The triaxial data are summarized in Table S3.

Table S2. Experimental data (connected porosity, permeability, Young's modulus, and uniaxial compressive strength) collected for this study. In total, 11 cylindrical samples (20 mm in diameter) were prepared from block CCC, and eight from blocks CC4A, CC4B, and CC10.

Sample	Connected porosity (%)	Permeability (m ²)	Young's modulus (GPa)	Uniaxial compressive strength (MPa)
CCC1*	14.8	9.36×10^{-15}	9.0	48.5
CCC2*	14.6	8.58×10^{-15}	9.9	51.8
CCC3*	15.3	1.29×10^{-14}	9.4	46.7
CCC4*	15.0	9.33×10^{-15}	9.0	46.3
CCC5*	15.1	1.05×10^{-14}	10.0	49.2
CCC6*	15.2	9.83×10^{-15}	9.3	46.8
CCC7*	15.8	1.02×10^{-14}	10.2	53.2
CCC8*	15.7	1.27×10^{-14}	9.5	47.6
CCC9*	15.5	1.08×10^{-14}	9.0	45.7
CCC10*	15.1	1.08×10^{-14}	8.9	44.5
CCC11*	14.5	7.06×10^{-15}	9.3	49.7
CC4A1**	7.4	8.08×10^{-18}	30.6	121.2
CC4A2**	7.9	4.65×10^{-18}	-	-
CC4A3**	9.8	8.69×10^{-18}	33.2	122.2
CC4A4**	15.6	2.32×10^{-17}	37.1	137.0
CC4A5**	13.9	1.51×10^{-18}	-	-
CC4A6**	14.6	1.11×10^{-17}	-	-
CC4A7**	11.1	3.82×10^{-17}	-	-
CC4A8**	11.9	2.59×10^{-18}	34.8	119.7
CC4B1*	13.9	1.59×10^{-16}	7.3	41.6
CC4B2*	13.8	1.50×10^{-15}	7.1	38.6
CC4B3*	12.5	7.08×10^{-15}	7.6	38.5
CC4B4	12.6	1.33×10^{-16}	9.4	49.2
CC4B5	11.8	1.02×10^{-16}	-	-
CC4B6	13.7	3.17×10^{-16}	-	-
CC4B7	12.8	2.40×10^{-16}	-	-
CC4B8	14.0	1.21×10^{-16}	-	-
CC10_1*	13.4	1.84×10^{-14}	8.0	38.5
CC10_2*	12.8	9.72×10^{-15}	9.6	48.2
CC10_3*	13.6	1.18×10^{-14}	9.0	47.5
CC10_4*	13.3	9.48×10^{-15}	9.3	42.3
CC10_5*	14.2	9.39×10^{-15}	-	-
CC10_6*	14.2	1.66×10^{-14}	-	-
CC10_7*	12.8	9.74×10^{-15}	-	-
CC10_8*	11.3	5.92×10^{-15}	-	-

* Forchheimer-corrected permeability, ** Klinkenberg-corrected permeability

To calculate the cohesion and the internal friction angle, the data from the triaxial experiments were plotted on a graph of maximum shear stress, τ_m where $\tau_m = (\sigma_1 - \sigma_3)/2$, as a function of mean normal stress, σ_m where $\sigma_m = (\sigma_1 + \sigma_3)/2$ (Labuz and Zang, 2012). A best-fit linear regression to these data, $\tau_m = e \cdot \sigma_m + f$, provides the two fitting parameters, e and f , required to calculate the cohesion and friction angle. The friction angle (in radians), ϕ_f , and the cohesion, C , are then given by $\phi_f = \sin^{-1}e$ (to convert the friction angle to degrees, the value is simply divided by $(\pi \times 180)$) and $C = \frac{f}{\cos\phi_f}$, respectively.

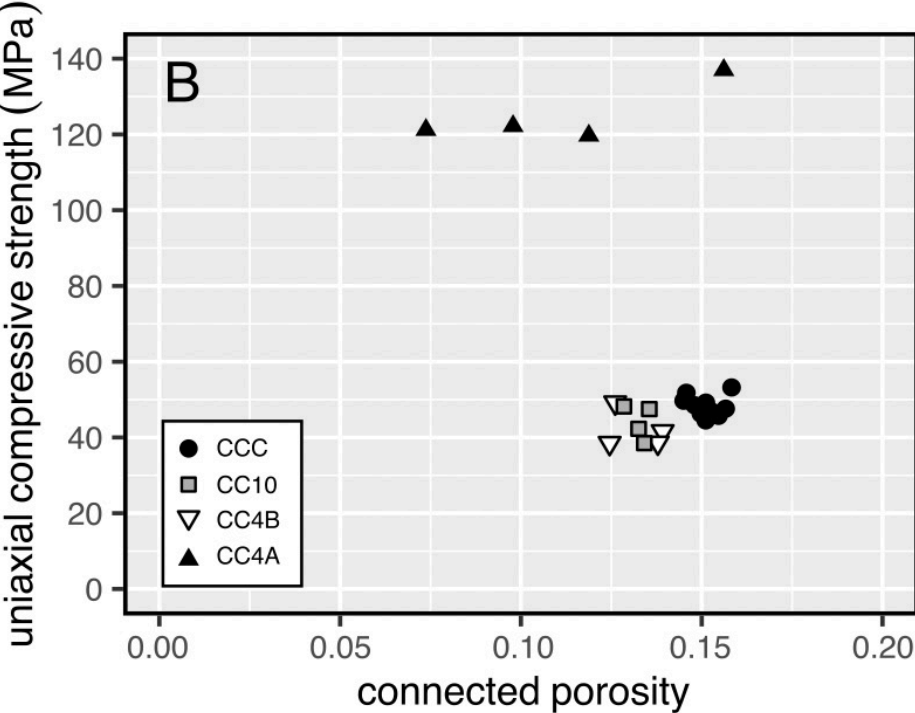
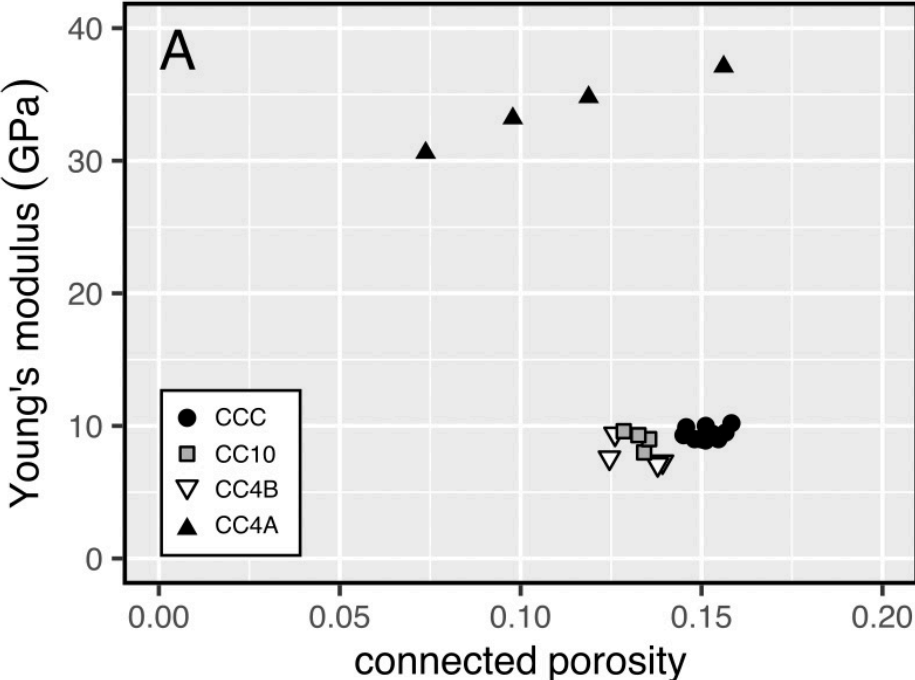


Figure S5. A: Young’s modulus as a function of connected porosity for the samples collected from Chaos Crags (Lassen Volcanic Center, USA). B: Uniaxial compressive strength (UCS) as a function of connected porosity for the samples collected from Chaos Crags.

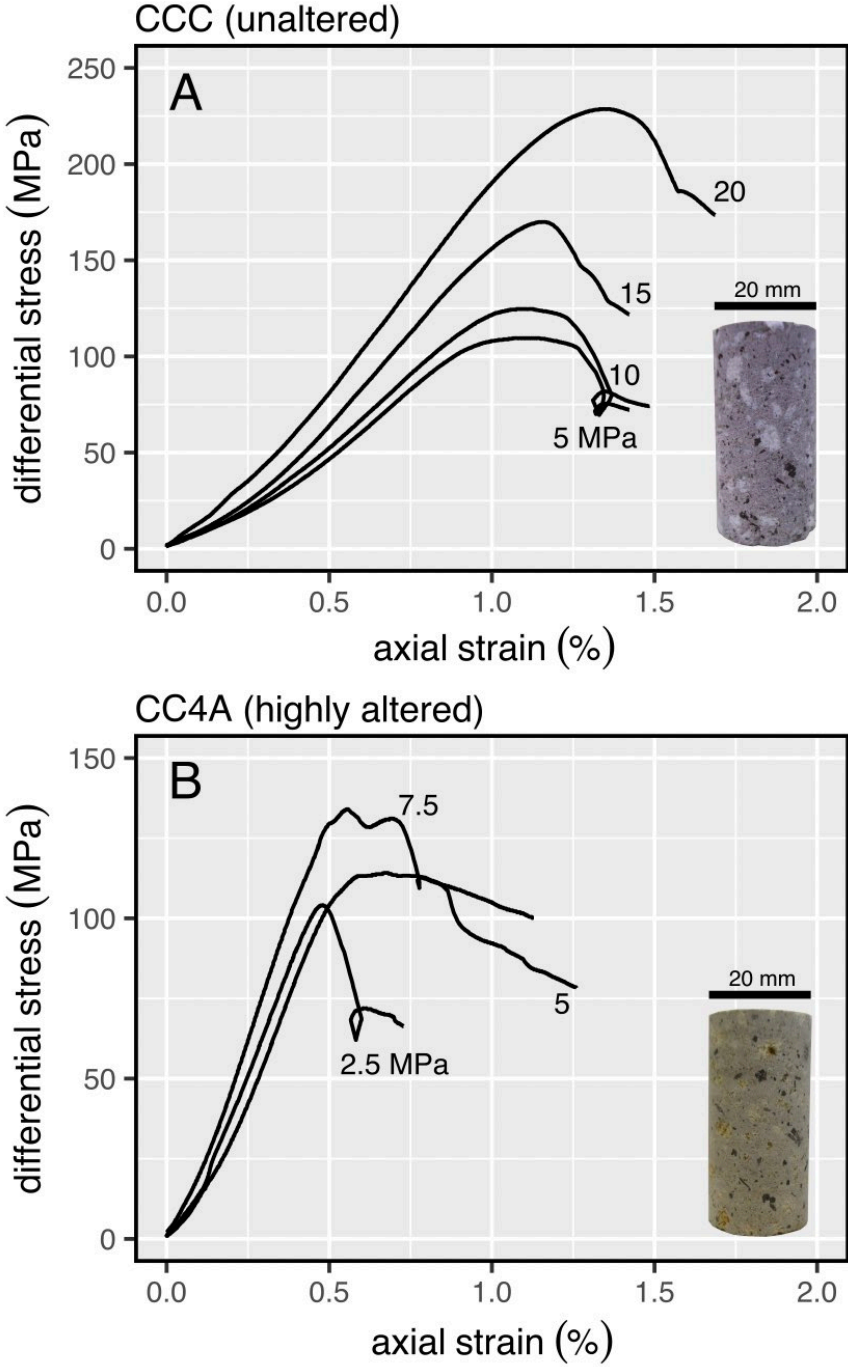


Figure S6. A: Triaxial stress-strain curves for samples of CCC deformed at different effective pressures (data from Ryan et al., 2020). The effective pressure is indicated next to each curve. Inset shows a photograph of an intact sample of CCC. B: Triaxial stress-strain curves for samples of CC4A deformed at different effective pressures. The effective pressure is indicated next to each curve, which represent separate experiments on an individual core samples (see Table S3). Inset shows a photograph of an intact sample of CC4A.

Table S3. Summary of the triaxial data (Fig. S6). Asterisk denotes data from Ryan et al. (2020). The samples from Ryan et al. (2020), labelled DAC, are cylinders cored from a block collected adjacent to block CCC (from the Chaos Jumbles deposit). Samples taken from block CC4A are the same as those listed in Table S2.

Sample	Connected porosity (%)	Pore fluid pressure (MPa)	Confining pressure (MPa)	Effective pressure (MPa)	Peak differential stress (MPa)
DAC2*	11.9	10	15	5	228.6
DAC3*	13.8	10	20	10	169.9
DAC4*	12.0	10	25	15	124.7
DAC5*	11.5	10	30	20	109.5
CC4A6	14.6	10	12.5	2.5	104.1
CC4A5	13.9	10	15	5	114.2
CC4A7	11.1	10	17.5	7.5	134.0

6. Upscaling the laboratory values

It is well known that laboratory-measured rock physical properties require upscaling to be used in large-scale modeling. The laboratory-scale Young's modulus was upscaled as described in Heap et al. (2020), taking a Geological Strength Index (GSI) of 55. A GSI of 55 was considered an "reasonable average" for lavas and lava flow breccias by Heap et al. (2020), based on a review of the published values and tables of GSI for volcanic rock masses (see Heap et al., 2020). Sample-scale Poisson's ratio was assumed to be 0.21 (see Heap et al., 2020) and upscaled (also using a GSI of 55) as described in Heap et al. (2020). The cohesion and angle of internal friction were upscaled by transforming the generalized form of the Hoek-Brown failure criterion to the Mohr-Coulomb failure criterion, explained below.

In order to upscale the laboratory strength data to the volcano scale, we used the generalized form of the Hoek-Brown failure criterion (Equation (1)) for fractured rock masses (as in Eberhardt, 2012). The variables in Equation (1) are a combination of laboratory strength measurements (C_o = uniaxial compressive strength, in MPa) and unitless empirical fitting parameters, m_b (Equation (2)), s (Equation (3)), and a (Equation (4)).

$$\sigma'_1 = \sigma'_3 + C_o \left(m_b \frac{\sigma'_3}{C_o} + s \right)^a \quad (1)$$

$$m_b = m_i e^{\left(\frac{GSI-100}{28-14D} \right)} \quad (2)$$

$$s = e^{\left(\frac{GSI-100}{9-3D} \right)} \quad (3)$$

$$a = \frac{1}{2} + \frac{1}{6} \left(e^{-\frac{GSI}{15}} + e^{-\frac{20}{3}} \right) \quad (4)$$

The unitless empirical fitting parameter m_i was derived from fitting the intact rock version of the Hoek-Brown failure criterion (Equation (5)) to laboratory triaxial testing (according to

Hoek and Brown, 1997) using RocData (Rocscience; <https://www.rocscience.com>). Empirical fitting parameter m_i was determined to be 43 and 17 for blocks CCC and CC4A, respectively. The unitless GSI was estimated as 55 following the recommendation of Heap et al. (2020) to characterize the structure and nature of the fractures in a typically fractured volcanic rock mass, and D was set to 0 for undamaged rock.

$$\sigma'_1 = \sigma'_3 + C_o \left(m_b \frac{\sigma'_3}{C_o} + s \right)^a \quad (5)$$

To provide rock mass input parameters for the Drucker-Prager failure criterion used by LaMEM, we transformed the Hoek-Brown failure criterion to the Mohr-Coulomb failure criterion according to Hoek et al. (2002). Using this transformation, we obtained the internal friction angle (Equation (6)) and cohesion, c , (Equation (7)) in MPa.

$$\phi = \sin^{-1} \left[\frac{6am_b(s+m_b\sigma_{3n})^{a-1}}{2(1+a)(2+a)+6am_b(s+m_b\sigma_{3n})^{a-1}} \right] \quad (6)$$

$$c = \frac{\sigma_{ci}[(1+2a)s+(1-a)m_b\sigma_{3n}](s+m_b\sigma_{3n})^{a-1}}{(1+a)(2+a)\sqrt{1+(6am_b(s+m_b\sigma_{3n})^{a-1})/((1+a)(2+a))}} \quad (7)$$

Where

$$\sigma_{3n} = \sigma_{3max}/\sigma_{ci} \quad (8)$$

$$\sigma_{3max} = 0.72\sigma_{cm} \left(\frac{\sigma_{cm}}{\gamma h} \right)^{-0.91} \quad (9)$$

$$\sigma_{cm} = \sigma_{ci} \cdot \frac{(m_b+4s-a(m_b-8s))(m_b/4+s)^{a-1}}{2(1+a)(2+a)} \quad (10)$$

The input parameters for Equations (8)-(10) derive from laboratory values (i.e. $\sigma_{ci} = C_0 =$ UCS) and unit weight (in kN/m³) or the empirical factors from Equations (2)-(4). However, one parameter must be linked to the geometry of the problem (Hoek et al., 2002): h , the height of the slope in question. Because of the large scale of the volcano (2000 m from base to peak), the selection of h affects the computed cohesion and internal friction angle. We decided to take the halfway point between the peak of the volcano and the top of the undeformable zone (the base) in our model (i.e. $h = 1000$ m).

7. Extended description of LaMEM

We used the hydro-thermo-mechanical modeling code LaMEM (Lithosphere and Mantle Evolution Model; Kaus et al., 2016), which models the non-linear, visco-elastoplastic deformation of rocks. LaMEM is an open-source software actively being developed at JGU

Mainz (Germany) (<https://bitbucket.org/bkaus/lamem/src/master/>). The modeling performed for this study was performed in two dimensions.

Mathematically, the model solves a coupled system of conservation equations, the conservation equations of momentum and mass. We refer the reader to Kaus et al. (2016) for a more detailed description. The various deformation mechanisms are connected in an additive constitutive relationship, where the total strain rate is the sum of the individual strain rates of elastic, viscous, and plastic deformation. Currently, LaMEM incorporates the Drucker-Prager failure criterion, which determines the magnitude of the plastic strain rate. The yield criterion has the form:

$$\tau_{II} \leq \sin(\phi) (p - p_f) + \cos(\phi) c \quad (11)$$

where τ_{II} is the second invariant of the deviatoric stress tensor, ϕ is the friction angle, c is the cohesion, and p and p_f are the dynamic and pore fluid pressure, respectively. The model describes the pore fluid pressure as a function of limiting hydrostatic, p_h , and lithostatic pressure, p_{lith} , such that:

$$p_f = p_h + \lambda_i (p_{lith} - p_h) \quad (12)$$

We therefore define a pore fluid pressure ratio, λ_i , which can be treated as a rock property in the individual deformable domains (Baumann et al., 2018). Pore fluid pressures are therefore limited between hydrostatic and lithostatic in our modeling. The internal free surface is used as the reference surface for determining hydrostatic pressure, and we assume plain strain in two dimensions. We highlight that, although our permeability measurements served to justify increasing the pore pressure within the altered zone, permeability values were not used as model input parameters.

Numerically, LaMEM uses staggered-grid finite differences for discretization (Harlow and Welch, 1965) and a marker-and-cell method (Harlow and Welch, 1965) to assign and track rock properties within a Eulerian advection framework. This approach enables us to model large deformation, as in salt tectonics (Baumann et al., 2017) or continental collision models (Pusok et al., 2015), where at each time step the discretized coupled system of equations is solved using the PETSc SNES framework (Balay et al., 2017). The ability to model large deformations is seen here as an advantage of LaMEM over commonly-used commercial packages such as FLAC (by Itasca Consulting Group; <https://www.itasca.com>), RS2 (by Rocscience; <https://www.rocscience.com>), and PLAXIS 2D (by Virtuosity; <https://www.virtuosity.com>). LaMEM accounts for topography with an internal free surface and a stabilized “sticky air” approach (Duretz et al., 2011; Kaus et al., 2010). For the topography of the volcano, we use a rectilinear finite differences grid, which is rectangular. We also use an internal boundary that is advected, a benchmarked approach widely used in the geodynamics community.

We model total displacement field and displacement vectors after 500 years for each of the four modeled scenarios (see the thumbnails in Fig. 2 in the manuscript). The reason for choosing 500 years is twofold. First, as the models are dynamic, we must decide when the

models reach a quasi-steady state and can be compared (see Baumann and Kaus, 2015). Here, we stop the models after 500 years, following an initial deformation phase that is dominated by an elastic response. Second, 500 years is a time interval of interest for large flank collapses, which typically occur at active every < 1000 years (see, for example, Siebert, 1987).

8. Models using different pore pressure ratios and no-slip boundary conditions

In the main manuscript, we present modeling using a pore fluid pressure ratio, λ_i , of 0.2 for the unaltered gray zone and 0.4 for the yellow altered zone (see volcano thumbnails in Figure S7). Due to the uncertainty in the pore pressure ratios found in nature, we present here ancillary modeling, using the free-slip boundary condition, in which we used pore pressure ratios for the unaltered and altered zones of 0.4 and 0.8, respectively. The results are presented in Figures S7A-D. These results show that the deformation pattern is the same (downward movement of the high central portion of the volcano and the lateral spreading of the flanks), but that volcano deformation is higher in the scenario in which the pore pressure ratio is increased from 0.4 to 0.8 (Figures S7A-D) than the scenario in which the pore pressure ratio is increased from 0.2 to 0.4 (Figure 2 in the main manuscript). Therefore, if alteration is able to significantly increase the pore pressure within the volcano, volcano deformation, and the likelihood of the associated hazards, will increase.

We present modeling using a free-slip boundary condition in the main manuscript (see Figure 2), assuming that the rocks forming the edifice are weaker than those forming the basement. Although we consider this the most likely scenario, because volcanic edifices typically haphazardly constructed from heterogeneous materials that are influenced by alteration and thermal and mechanical stressing, it is likely that, in nature, the boundary condition between the edifice and the volcano basement exists somewhere between the free-slip and no-slip boundary endmembers (van Wyk de Vries and Borgia, 1996). Based on this, we have performed an additional suite of models in which we used a no-slip boundary (Figure S7E-H), to see if the deformation patterns differ significantly. The pore pressure ratios used in these models were 0.4 and 0.8 for the unaltered and altered zones, respectively. Figure S7 shows that the deformation patterns are somewhat similar between the free-slip and no-slip boundary condition endmembers, although deformation is largely restricted to the flanks. These simulations show that, regardless of the boundary condition, pockets of high pore fluid pressure will increase volcano deformation and increase volcanic instability. We highlight, however, that the magnitude of the displacement is higher in the free-slip condition. The maximum displacements in the free-slip and no-slip boundary conditions are 100 and 40 m, respectively (Figure S7). As stated above, it is likely that the displacement resulting from pore pressurization in nature is in between these endmember values. These models highlight that the coupling and strength difference between the edifice and the basement rocks plays a role in dictating large-scale volcano deformation (as discussed in van Wyk de Vries and Borgia, 1996, and other papers by these authors).

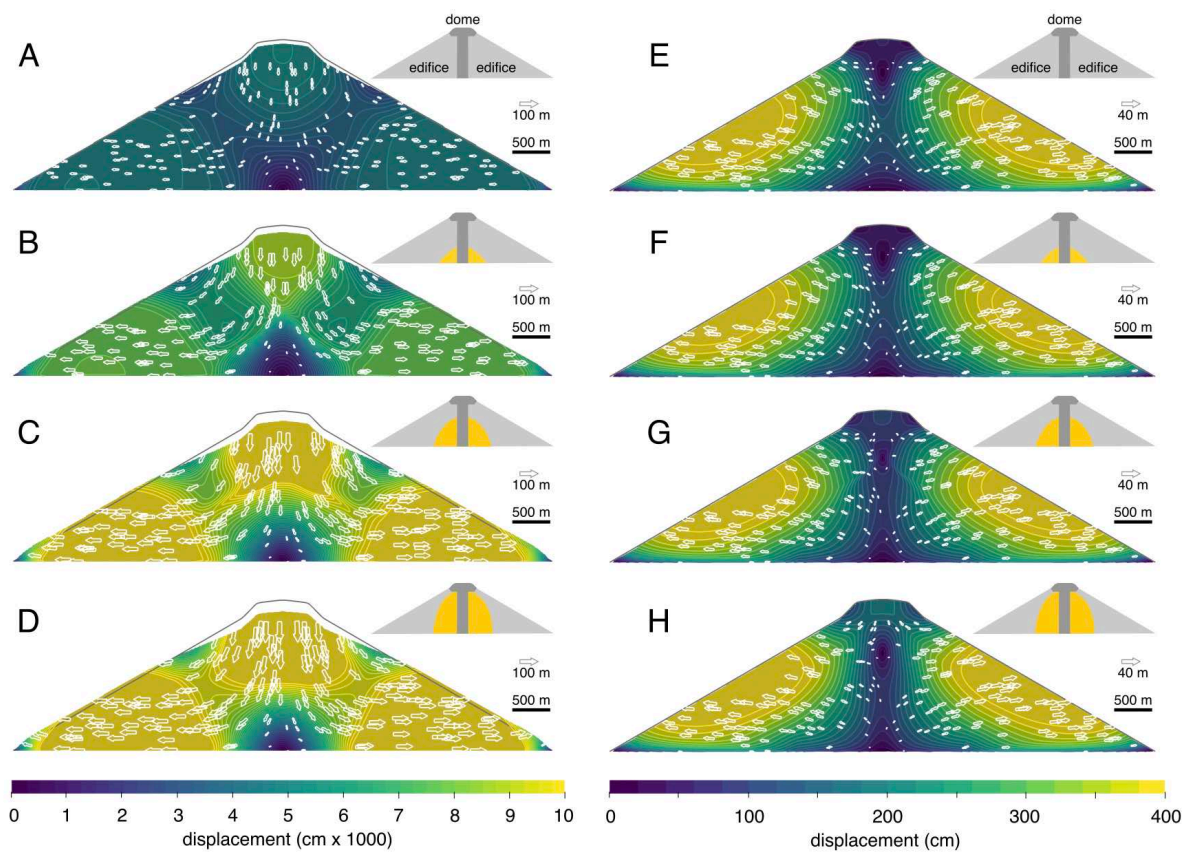


Figure S7. Results of the large-scale volcano stability modeling (using hydro-thermo-mechanical modeling code LaMEM) using a pore fluid pressure ratio of 0.4 for the unaltered zone and 0.8 for the altered zone (see thumbnails) for the free-slip boundary condition (panels A-D) and the no-slip boundary condition (panels E-H). Colors indicate the total displacement field (blue and yellow colors indicate low and high displacement, respectively) and the white arrows show the displacement vectors. Models were run for 500 years. Thumbnails show the model setup, where light and dark gray zones are unaltered zones and the yellow zones are altered zones with a high pore pressure. A: Homogeneous volcano. B: Volcano with a small alteration zone. C: Volcano with the medium alteration zone. D: Volcano with a large alteration zone.

9. References

- Balay, S., Abhyankar, S., Adams, M., Brown, J., Brune, P., Buschelman, K., ... & Knepley, M., 2017. PETSc Users Manual Revision 3.8 (No. ANL-95/11 Rev 3.8). Argonne National Lab. (ANL), Argonne, IL (United States).
- Baumann, T. S., & Kaus, B. J. (2015). Geodynamic inversion to constrain the non-linear rheology of the lithosphere. *Geophysical Journal International*, 202(2), 1289-1316.
- Baumann, T. S., Kaus, B. J. P., & Eichheimer, P. (2017, June). 3D numerical modelling of salt tectonics. In 79th EAGE Conference and Exhibition 2017 (Vol. 2017, No. 1, pp. 1-5). European Association of Geoscientists & Engineers.
- Baumann, T. S., Kaus, B. J., & Popov, A. A. (2018). Deformation and stresses related to the Gorleben salt structure: insights from 3d numerical models. *Mechanical Behavior of Salt, Saltmech IX*, 15-27.
- Bauville, A., & Baumann, T. S. (2019). geomIO: An Open-Source MATLAB Toolbox to Create the Initial Configuration of 2-D/3-D Thermo-Mechanical Simulations From 2-D Vector Drawings. *Geochemistry, Geophysics, Geosystems*, 20(3), 1665-1675.
- Bergmann, J., Friedel, P., & Kleeberg, R. (1998). BGMN—a new fundamental parameters based Rietveld program for laboratory X-ray sources, its use in quantitative analysis and structure investigations. *CPD Newsletter*, 20(5).
- Doebelin, N., & Kleeberg, R. (2015). Profex: a graphical user interface for the Rietveld refinement program BGMN. *Journal of applied crystallography*, 48(5), 1573-1580.
- Duretz, T., Gerya, T. V., & May, D. A. (2011). Numerical modelling of spontaneous slab breakoff and subsequent topographic response. *Tectonophysics*, 502(1-2), 244-256.
- Eberhardt E (2012) The Hoek–Brown failure criterion. *Rock Mech Rock Eng* 45:981–988. DOI 10.1007/s00603-012-0276-4
- Farquharson, J. I., Baud, P., & Heap, M. J. (2017). Inelastic compaction and permeability evolution in volcanic rock. *Solid Earth*, 8(2), 561-581.
- Harlow, F. H., & Welch, J. E., 1965. Numerical calculation of time-dependent viscous incompressible flow of fluid with free surface. *The physics of fluids*, 8(12), 2182-2189.
- Heap, M. J., Lavallée, Y., Petrakova, L., Baud, P., Reuschlé, T., Varley, N. R., & Dingwell, D. B. (2014). Microstructural controls on the physical and mechanical properties of edifice-forming andesites at Volcán de Colima, Mexico. *Journal of Geophysical Research: Solid Earth*, 119(4), 2925-2963.
- Heap, M. J., & Kennedy, B. M. (2016). Exploring the scale-dependent permeability of fractured andesite. *Earth and Planetary Science Letters*, 447, 139-150.
- Heap, M. J., Kushnir, A. R., Gilg, H. A., Wadsworth, F. B., Reuschlé, T., & Baud, P. (2017). Microstructural and petrophysical properties of the Permo-Triassic sandstones (Buntsandstein) from the Soultz-sous-Forêts geothermal site (France). *Geothermal Energy*, 5(1), 1-37.
- Heap, M. J., Villeneuve, M., Albino, F., Farquharson, J. I., Brothelande, E., Amelung, F., ... & Baud, P. (2020). Towards more realistic values of elastic moduli for volcano modelling. *Journal of Volcanology and Geothermal Research*, 390, 106684.
- Hoek E, Brown ET (1997) Practical estimates of rock mass strength. *International journal of rock mechanics and mining sciences*, 34, 1165-1186.
- Hoek E, Carranza-Torres CT, Corkum B (2002) Hoek–Brown failure criterion—2002 edition. In: Hammah R, Bawden W, Curran J, Telesnicki M (eds) *Proceedings of the Fifth North American Rock Mechanics Symposium (NARMS-TAC)*, University of Toronto Press, Toronto: 267-273.
- Kaus, B. J., Mühlhaus, H., & May, D. A. (2010). A stabilization algorithm for geodynamic numerical simulations with a free surface. *Physics of the Earth and Planetary Interiors*, 181(1-2), 12-20.
- Kaus, B., Popov, A. A., Baumann, T., Pusok, A., Bauville, A., Fernandez, N., & Collignon, M. (2016, February). Forward and inverse modelling of lithospheric deformation on geological timescales. In *Proceedings of NIC Symposium*.
- Labuz, J. F., & Zang, A. (2012). Mohr–Coulomb failure criterion. In *The ISRM Suggested Methods for Rock Characterization, Testing and Monitoring: 2007-2014* (pp. 227-231). Springer, Cham.

- Pusok, A. E., & Kaus, B. J. (2015). Development of topography in 3-D continental-collision models. *Geochemistry, Geophysics, Geosystems*, 16(5), 1378-1400.
- Ryan, A. G., Heap, M. J., Russell, J. K., Kennedy, L. A., & Clynne, M. A. (2020). Cyclic shear zone cataclasis and sintering during lava dome extrusion: Insights from Chaos Crags, Lassen Volcanic Center (USA). *Journal of Volcanology and Geothermal Research*, 401, 106935.
- Siebert, L. (1984). Large volcanic debris avalanches: characteristics of source areas, deposits, and associated eruptions. *Journal of Volcanology and Geothermal Research*, 22(3-4), 163-197.
- van Wyk de Vries, B., & Borgia, A. (1996). The role of basement in volcano deformation. Geological Society, London, Special Publications, 110(1), 95-110.